Metallographic cooling rates of the IIIAB iron meteorites

Jijin Yang [*], Joseph I. Goldstein

Department of Mechanical and Industrial Engineering, University of Massachusetts, Amherst, MA 01003, USA

Received 3 January 2006; accepted in revised form 4 April 2006

Abstract

An improved computer simulation program has been developed and used to re-measure the metallographic cooling rates of the IIIAB irons, the largest iron meteorite chemical group. The formation of this chemical group is attributed to fractional crystallization of a single molten metallic core during solidification. Group IIIAB irons cooling rates vary by a factor of 6 from 56 to 338 °C/My. The cooling rate variation for each meteorite is much smaller than in previous studies and the uncertainty in the measured cooling rate for each meteorite is greatly reduced. The lack of correction for the orientation of the kamacite–taenite interface in the cooling rate measurement of a given meteorite in previous studies not only leads to large cooling rate variations but also to inaccurate and low cooling rates. The cooling rate variation with Ni content in the IIIAB chemical group measured in this study is attributable, in part, to the variation in nucleation temperature of the Widmanstatten pattern with Ni content and nucleation mechanism. However, the factor of 6 variation in cooling rate of the IIIAB irons is hard to explain unless the IIIAB asteroidal core was exposed or partially exposed in the temperature range in which the Widmanstatten pattern formed. Measurements of the size of the island phase in the cloudy zone of the taenite phase and Re–Os data from the IIIAB irons and the pallasites make it hard to reconcile the idea that pallasites are located at the boundary of the IIIAB asteroid core.
© 2006 Elsevier Inc. All rights reserved.

1. Introduction

Chemical element distribution patterns in IIIAB meteorites, the largest iron meteorite chemical group, are attributed to the fractional crystallization of a single molten metallic core during solidification (Scott, 1972). If one assumes that the structure and size of the IIIAB parent body did not change significantly during cooling, the IIIAB irons are fragments of a single core which had the same cooling rate at any temperature. Only a few systematic investigations of the metallographic cooling rates of the IIIAB have been undertaken. The two earliest studies are based on the kamacite bandwidth method (Goldstein and Short, 1967) and showed that the metallographic cooling rates vary by a factor of 10 (Goldstein and Short, 1967) and by a factor of 9 (Narayan and Goldstein, 1985). The measured cooling rates decrease with increasing Ni content in the low Ni portion of the chemical group (IIIA irons). Based on the measured cooling rates, it was suggested that IIIAB irons did not form in a single

core, although the IIIAB irons may have developed in a single parent body. In the most recent study, Rasmussen (1989) re-measured the metallographic cooling rate of the IIIAB irons based on the Wood method (Wood, 1964). Although the measured cooling rates in the IIIAB irons vary by a factor of 9, Rasmussen concluded that the cooling rate of the IIIAB irons was constant throughout the chemical group. We suggest that a variation of a factor of 9 in the cooling rate is much too large to conclude that the IIIAB irons have a constant cooling rate.

In the last few years, the interdiffusion coefficients for the kamacite and taenite phases of the Fe–Ni system have been re-evaluated (Yang and Goldstein, 2004) and the formation mechanism and the nucleation temperature of the Widmanstatten structure (Yang and Goldstein, 2005) have been determined. These recent advances allow for a major improvement in the computer simulation program which is the heart of the metallographic cooling rate method. In this paper, we use an improved computer simulation program to re-measure the cooling rates of the IIIAB irons. In addition, the orientation of the kamacite–taenite interface to the sample surface was measured in order to obtain the cor-

---

[*] Corresponding author.
  E-mail addresses: jiyang@ecs.umass.edu, jig0@ecs.umass.edu (J. Yang).

rect value of the taenite half-width for application of the Wood method. More accurate cooling rates are measured with better precision which in turn allows for an improved understanding of the relation between the IIIAB irons and their parent asteroidal body.

2. Method for measuring metallographic cooling rates

2.1. Selection of IIIAB iron meteorites

The IIIAB irons that were studied are listed in Table 1. The meteorites span a range from the lowest Ni and P members to the highest Ni and P members of the IIIAB group. Because the largest cooling rate variations occur for the lower Ni members of IIIAB ($\sim < 8.5$ wt%Ni) (Goldstein and Short, 1967; Rasmussen, 1989), we selected proportionally more low Ni members of the IIIAB chemical group for study.

2.2. Metallographic cooling rate model

The metallographic cooling rate model simulates the growth of the Widmanstatten pattern and the distribution of Ni content in the kamacite and taenite phases during the growth process. The model includes five major factors: the mechanism for Widmanstatten pattern formation, the kamacite nucleation temperature, the effect of impingement, the Fe–Ni and Fe–Ni–P phase diagrams, and the interdiffusion coefficients.

2.2.1. The Widmanstatten pattern formation mechanism, kamacite nucleation temperature and impingement

Yang and Goldstein (2005) have shown that three mechanisms or reactions are responsible for the formation of the Widmanstatten structure during cooling in IIIAB meteorites (Fig. 1). These mechanisms, reaction II
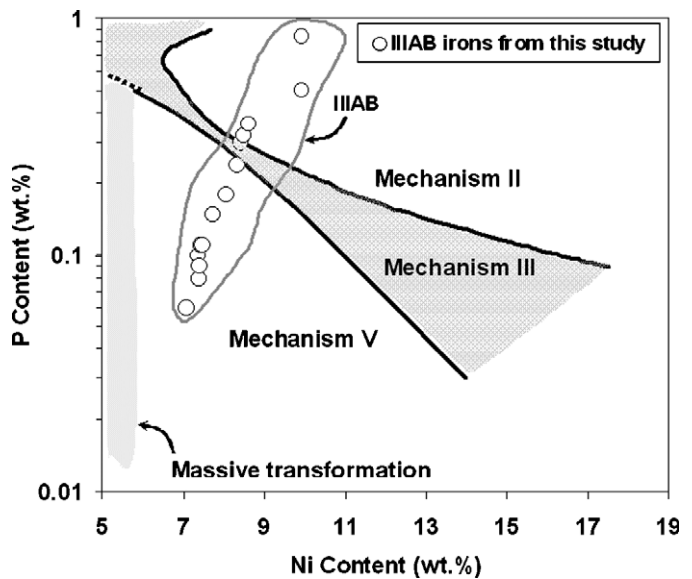

Fig. 1. Formation mechanism of the Widmanstatten pattern in chemical group IIIAB as a function of the bulk Ni and P content of the metal (Yang and Goldstein, 2005). The Ni and P contents of the IIIAB irons that were studied are also plotted.

($\gamma \rightarrow \gamma + Ph \rightarrow \alpha + \gamma + Ph$), where α is kamacite, γ is taenite and Ph is phosphide, reaction III ($\gamma \rightarrow (\alpha + \gamma) \rightarrow \alpha + \gamma + Ph$), and reaction V ($\gamma \rightarrow \alpha_2 + \gamma \rightarrow \alpha + \gamma$) where α_2 is martensite, depend on the bulk Ni and P content of the meteorites. For reactions II and III, the α-kamacite phase nucleates upon entering the $\alpha + \gamma + Ph$ three phase field during cooling. For reaction V, α_2-martensite nucleates at the martensite start temperature, M_s, during cooling and before the meteorite enters the $\alpha + \gamma + Ph$ three phase field. The α_2 phase subsequently decomposes into α-kamacite and γ-taenite and the resultant α grows into residual γ taenite.

Table 1
IIIAB irons analyzed in this study

Meteorite name	Source	Wt%Ni	Wt%P	W pattern mechanism	Kamacite nucleation temperature (°C)
Picacho	TCU M296.1	7.08[a]	0.06[a]	V	660
Haig	USNM 5710	7.34[a]	0.1[a]	V	655
Greenbrier County	USNM 1546	7.38[a]	0.08[a]	V	650
Livingston (Montana)	USNM 1703	7.4 [a]	0.09[a]	V	655
Davis Mt.	USNM 1443	7.41[a]	0.11[a]	V	650
Angelica	UMASS 2117	7.46[a]	0.11[a]	V	650
Casas Grandes	USNM 3696	7.72[a]	0.15[a]	V	640
Cumpas	USNM 1509	8.04[a]	0.18[a]	V	620
Uruachic	UNM I63.1	8.33[b]	0.24[d]	V	615
Point of Rocks	UNM I23.4	8.4[c]	0.3[d]	II	723
Drum Mt.	USNM 1417b	8.47[a]	0.32[d]	II	720
Spearman	UMASS	8.61[a]	0.36[a]	II	710
Chupaderos	FMNM ME1045	9.9[a]	0.5[a]	II	670
Bella Roca	FMNH 611	9.91[a]	0.85[a]	II	668

TCU, Texas Christian University; USNM, National Museum of Natural History; UMASS, University of Massachusetts; UNM, University of New Mexico; FMNH, Field Museum of Natural History.
[a] Buchwald (1975).
[b] Wasson et al. (1998).
[c] Goldstein (1969).
[d] Doan and Goldstein (1969).

For the five high Ni and high P IIIAB irons studied (Fig. 1), mechanism II is applicable. These meteorites are P saturated before kamacite nucleation occurs and the kamacite nucleates at the temperature where the meteorite cools through the $\gamma + Ph/\alpha + \gamma + Ph$ phase boundary. For the nine low Ni and low P IIIAB irons studied (Fig. 1), mechanism V is applicable. These meteorites are not P saturated before kamacite nucleation occurs and the kamacite nucleation temperature is M_s, the martensite start temperature. None of the meteorites selected for this study were located in the Ni–P composition region where mechanism III is applicable (Fig. 1). Table 1 lists the applicable mechanism for the formation of the Widmanstatten pattern in each of the IIIAB irons as well as the kamacite nucleation temperature.

Saikumar and Goldstein (1988) have shown that impingement plays an important role in the growth of the Widmanstatten pattern. The effect of impingement is to restrict the growth of kamacite and increase the amount of Ni in the taenite phase during the formation of the Widmanstatten pattern. Impingement is due to overlapping Ni gradients from the growth of adjacent kamacite plates. Impingement is considered in the computer simulation model by varying the distance, L, between adjacent kamacite nucleation sites. The Ni content vs. taenite half-width method (Wood, 1964), which includes the effect of impingement, will be used to obtain the IIIAB cooling rates.

2.2.2. Phase diagrams

The recent binary Fe–Ni binary phase diagram was determined by Yang et al. (1996), resulting in a major revision in the Fe–Ni phase diagram below 400 °C. However, the binary Fe–Ni phase diagram can only be used for cooling rate calculations in P-free metal, such as that found in the ordinary chondrites.

Metal in the iron and stony-iron meteorites contains minor amounts of elements such as P, S, C, etc. Of these minor elements, P has the most significant influence on the Fe–Ni phase diagram and the formation of the Widmanstatten pattern. In the IIIAB irons, the carbon content is low, about 0.01 wt% (Buchwald, 1975), and graphite and cohenite are rare or absent. The sulfur content in the metal is very low, about 10–100 ppm (Buchwald, 1975). Sulfide minerals, predominantly troilite, which are present as inclusions in taenite at high temperatures, contain almost all the sulfur that is present in the IIIAB irons. It is unlikely that either carbon or sulfur was present in sufficient quantities in the taenite phase to influence the formation of kamacite below 700 °C during the cooling process. We therefore assume that the Fe–Ni–P ternary phase diagram controls the nucleation and the equilibrium phase compositions of kamacite and taenite for the P-bearing metal phases in meteorites.

Fig. 2a shows a schematic isothermal section of the Fe-rich part of the ternary Fe–Ni–P phase diagram, Romig and Goldstein (1980). The nomenclature system of Moren and Goldstein (1979) is also shown in Fig. 2a and is used to
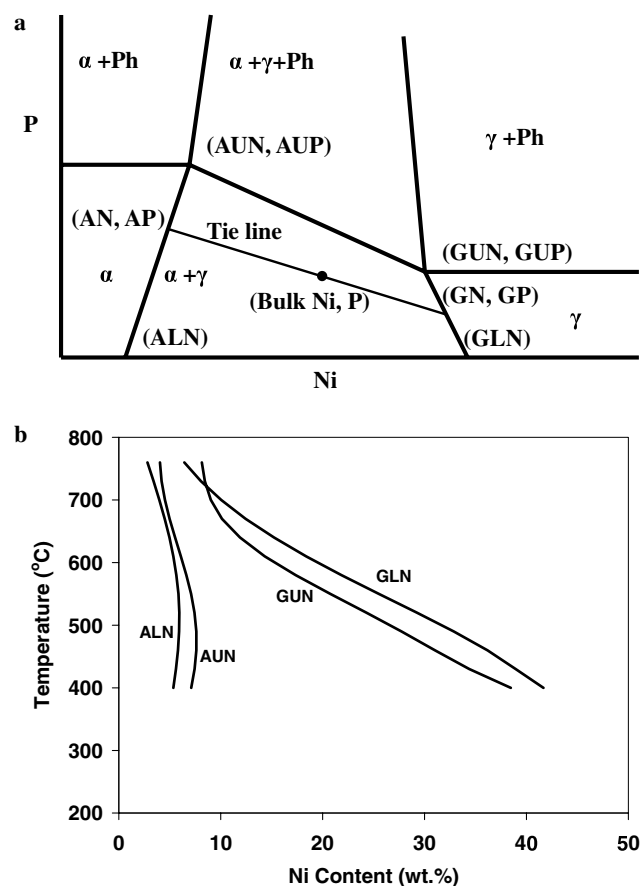

Fig. 2. (a) Schematic isothermal section of the Fe–Ni–P ternary phase diagram. (b) Binary Fe–Ni and pseudo-binary Fe–Ni (P sat.) phase diagrams between 750 and 400 °C. The nomenclature system of Moren and Goldstein (1979) is used.

describe phase boundaries for both the binary Fe–Ni and the ternary Fe–Ni–P systems. ALN and GLN represent the Ni content of the $\alpha/(\alpha + \gamma)$ and $(\alpha + \gamma)/\gamma$ boundaries in the Fe–Ni binary system. AUN and GUN represent the Ni content of the P saturated α and γ corners of the three phase field $\alpha + \gamma + Ph$. AN and AP represent the Ni and P contents, respectively, at the $\alpha/(\alpha + \gamma)$ phase boundary on a tie line with GN and GP which represent the Ni and P contents at the $\gamma/(\alpha + \gamma)$ phase boundary. AN, AP, GN, and GP lie on a tie line that goes through the bulk Ni and P content of the meteorite. AUP and GUP represent the P content of α and γ at the α and γ corners of the three phase $\alpha + \gamma + Ph$ field. Fig. 2b shows the binary Fe–Ni phase diagram (ALN, GLN) and the pseudo binary Fe–Ni (P saturated) phase diagram above 400 °C for the P saturated $\alpha/(\alpha + \gamma)$ and $(\alpha + \gamma)/\gamma$ boundaries (AUN, GUN) as a function of temperature. The experimentally determined pseudo binary Fe–Ni (P sat.) phase diagrams by Doan and Goldstein (1970) and Romig and Goldstein (1980, 1981) are used above the monotectoid temperature.

For the taenite boundary of the Fe–Ni (P sat.) phase diagrams at $\leqslant 400$ °C, Hopfe and Goldstein (2001) used the experimental value of 37.5 wt% Ni at 400 °C (Romig

and Goldstein, 1980, 1981) as the monotectoid composition in their pseudo binary Fe–Ni (P sat.) phase diagram for their cooling rate calculations. However, the monotectoid composition used by Hopfe and Goldstein (2001) is not consistent with the lower limit of the discontinuity in Ni concentration profile in taenite obtained by Yang et al. (1996, 1997a). The lower limit of the discontinuity in Ni concentration profile in taenite, which is 41.6 wt% Ni, is the monotectoid composition for the Fe–Ni (P sat.) system. We use the monotectoid composition of 41.6 wt% and the solubility of Ni, experimentally determined by Romig et al. (1980, 1981), in the γ phase from 850 to 300 C to determine the monotectoid temperature, which is ∼380 °C in the Fe–Ni (P sat.) phase diagram.

Below the monotectoid temperature, Hopfe and Goldstein (2001) used the metastable binary Fe–Ni and pseudo binary Fe–Ni (P sat.) phase diagrams to obtain the taenite Ni contents. Their calculated results for mesosiderites were inconsistent with the measured data for narrow taenite bands. Recently, Yang and Goldstein (2003) used the Fe–Ni equilibrium phase diagram below the monotectoid temperature. Their results for mesosiderites were consistent with the measured results for narrow taenite bands. Therefore, we will assume that the taenite interface composition for equilibrium with kamacite follows the equilibrium Fe–Ni phase diagram below the monotectoid temperature and for Ni contents of GUN and GLN up to ∼65 wt%.

The solvus lines ALN, AUN for the α/(α + γ) boundary and GLN, GUN for the (α + γ)/γ boundary are fit by polynomial equations and are shown in Fig. 3. Data used to develop the equations for the binary Fe–Ni phase diagram, ALN, GLN, are taken from Goldstein and Ogilvie (1965); Romig and Goldstein (1980) and Yang et al. (1996). Data used to develop the equations for the pseudo binary Fe–Ni (P sat.) phase diagram, AUN, GUN, are taken from Doan and Goldstein (1970); Romig and Goldstein (1980, 1981); Yang et al. (1996), and results of this paper. The polynomial equations for the solvus lines are of the form:

$$\text{Solvus line(wt\%Ni)} = \sum_{i=0}^{6} A_i T^i, \tag{1}$$

where T is temperature in degree centigrade. The constants A_i ($i = 0$–6) for ALN, AUN, GLN, and GUN (Figs. 2 and 3) are listed in Table 2.

The solubility of P in kamacite (AUP, $P_\alpha^{\text{Sol.}}$) and taenite (GUP, $P_\gamma^{\text{Sol.}}$) (Fig. 2a) was experimentally determined by Doan and Goldstein (1970) and Romig and Goldstein (1980). Clarke and Goldstein (1978) plotted the experimental data of Doan and Goldstein (1970) and showed that there is a linear relationship between the logarithm of the P solubility and the inverse of the absolute temperature. Saikumar and Goldstein (1988) used two equations to express the P solubility vs. temperature relationships. We have re-evaluated the experimental data and developed more accurate equations for AUP and GUP.
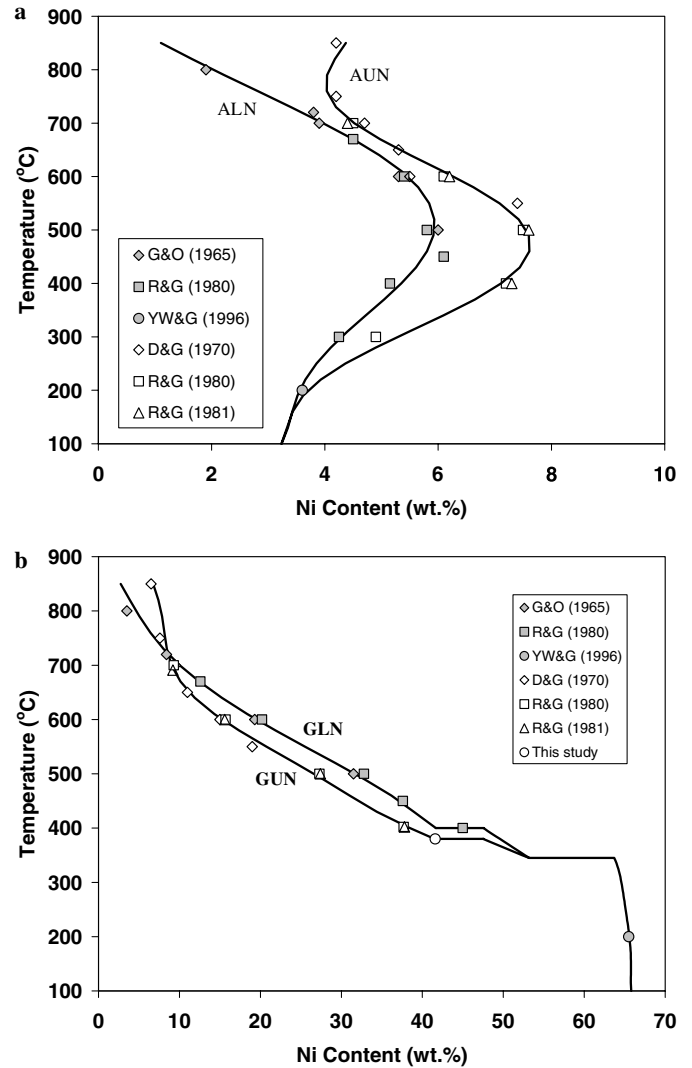

Fig. 3. (a) α/(α + γ) phase boundaries in the binary Fe–Ni system (ALN) and the pseudo-binary Fe–Ni (P sat.) system (AUN). (b) (α + γ)/γ phase boundaries in the binary Fe–Ni system (GLN) and the pseudo-binary Fe–Ni (P sat.) system (GUN). References: G&O, Goldstein and Ogilvie (1965); R&G, Romig and Goldstein (1980, 1981); YW&G, Yang et al. (1996); and D&G, Doan and Goldstein (1970).

$$\text{AUP}\left(P_\alpha^{\text{Sol.}}\right) = \exp(5.5\text{–}5961.0/T), \tag{2a}$$

$$\text{GUP}\left(P_\gamma^{\text{Sol.}}\right) = \exp(5.3\text{–}6504.0/T). \tag{2b}$$

The temperature T is given in K. Fig. 4 shows a comparison of AUP and GUP from Eqs. (2a), (2b) and AUP and GUP from Saikumar and Goldstein (1988).

The high Ni and P members and the low Ni and P members of the IIIAB irons do not follow the same phase boundary during the kamacite nucleation and growth process. For high P members of IIIAB irons (Point of Rocks, Drum Mt., Spearman, Chupaderos and Bella Roca), taenite is P saturated at high temperatures and kamacite nucleates and grows by mechanism II, Yang and Goldstein (2005). Kamacite nucleates at the P saturated γ/(α + γ) boundary, GUN (Fig. 3b) and the α and γ boundaries of

Table 2
Constants for polynomial fit of ALN, AUN, GLN, and GUN in the Fe–Ni and Fe–Ni–P systems

| Solvus line	A_0	A_1	A_2	A_3	A_4	A_5	A_6
$\alpha/(\alpha + \gamma)$							
ALN (850–100 °C)	1.4004	4.0945×10^{-2}	-3.3992×10^{-4}	1.373×10^{-6}	-2.5332×10^{-9}	2.1113×10^{-12}	-6.5531×10^{-16}
$\alpha/(\alpha + \gamma)$ (P saturated)							
AUN (850–100 °C)	0.4545	7.1252×10^{-2}	-6.9206×10^{-4}	3.1769×10^{-6}	-6.6215×10^{-9}	6.2552×10^{-12}	-2.1918×10^{-16}
$(\alpha + \gamma)/\gamma$							
GLN (850–400 °C)	-217.6637	1.8956	-4.8019×10^{-3}	4.9177×10^{-6}	-1.8038×10^{-9}	—	—
$(\alpha + \gamma)/\gamma$							
GLN (400–345 °C)	88.9545	-0.1036	—	—	—	—	—
$(\alpha + \gamma)/\gamma$							
GLN (345–100 °C)	73.2034	-0.2116	2.295×10^{-3}	-1.1763×10^{-5}	2.84×10^{-8}	-2.6388×10^{-11}	—
$(\alpha + \gamma)/\gamma$ (P saturated)							
GUN (850–380 °C)	3176.0494	-31.5804	0.13102	-2.8544×10^{-4}	3.4274×10^{-7}	-2.1498×10^{-10}	5.5091×10^{-14}
$(\alpha + \gamma)/\gamma$ (P saturated)							
GUN (380–345 °C)	109.3857	-0.1629	—	—	—	—	—
$(\alpha + \gamma)/\gamma$ (P saturated)							
GUN (345-100 °C)	73.2034	-0.2116	2.295×10^{-3}	-1.1763×10^{-5}	2.84×10^{-8}	-2.6388×10^{-11}	—
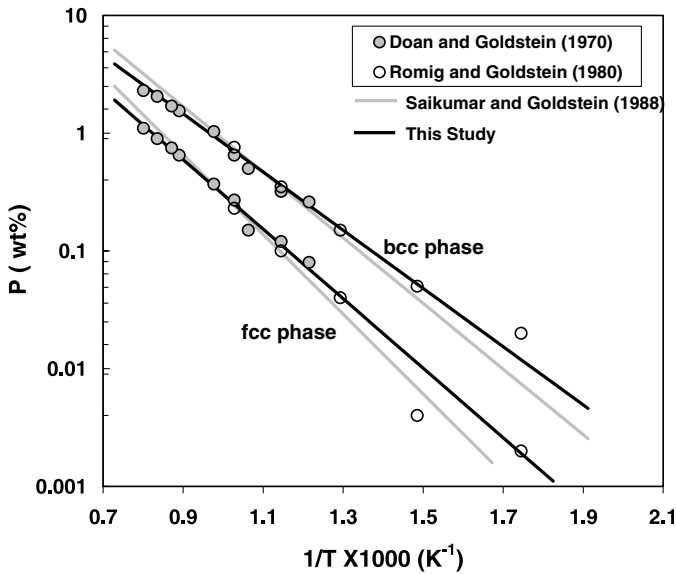
Fig. 4. Solubility of P in kamacite (AUP) and taenite (GUP) as a function of temperature. Experimental data are also plotted.

the pseudobinary Fe–Ni (P sat.) phase diagram (AUN, GUN) (Fig. 3) are used in the metallographic cooling rate model.

For the low Ni and P members of chemical group IIIAB, taenite is not P saturated at high temperatures and kamacite nucleates and grows by mechanism V, in which kamacite nucleates at the martensite start temperature and the α_2-martensite is not saturated in P. The $\alpha/(\alpha + \gamma)$ phase boundary (AN, AP) lies between ALN and AUN and the $\gamma/(\alpha + \gamma)$ phase boundary (GN, GP) lies between GLN and GUN on a tie line that goes through the bulk Ni and P content of the meteorite (Fig. 2a). The values of AN, AP, GN, and GP (Fig. 2a) are determined using the methodology developed by Moren and Goldstein (1979). The low P members of chemical group IIIAB enter

the three phase region $\alpha + \gamma + Ph$ in the pseudo-binary Fe–Ni (P sat.) phase diagram (Fig. 2b) at low temperatures and follow AUN and GUN on further cooling. Fig. 5 shows the $\alpha/(\alpha + \gamma)$ phase boundaries (AUN, ALN, and AN) for the 14 IIIAB irons as a function of temperature during the formation of the Widmanstatten pattern.

2.2.3. Diffusion coefficients

Kamacite diffusion coefficients for the binary Fe–Ni system have been determined experimentally (Hirano et al., 1961; Borg and Lai, 1963; Goldstein et al., 1965; Dean and Goldstein, 1986; Cermak et al., 1989). The data are plotted in Fig. 6 and show a subtle but real decrease in the log D vs. $1/T$ relationship below the Curie temperature.
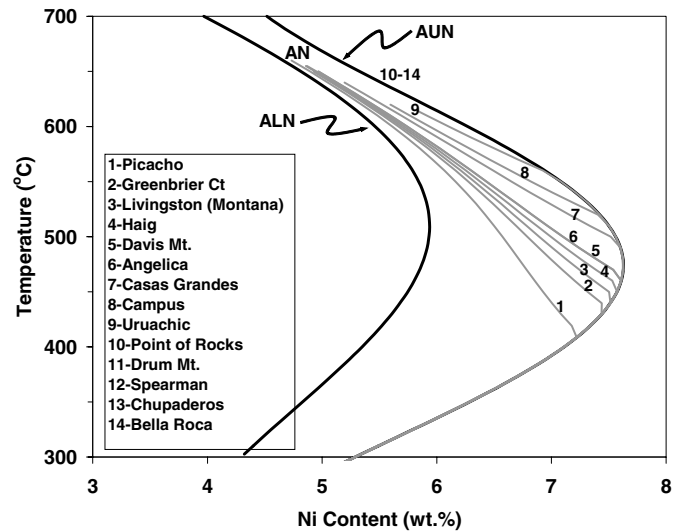

Fig. 5. $\alpha/(\alpha + \gamma)$ phase boundary values (ALN, AN, and AUN) as a function of temperature during the formation of the Widmanstatten pattern for the 14 IIIAB irons. The Widmanstatten pattern forms by mechanism V for meteorites 1–9 and by mechanism II for meteorites 10–14.
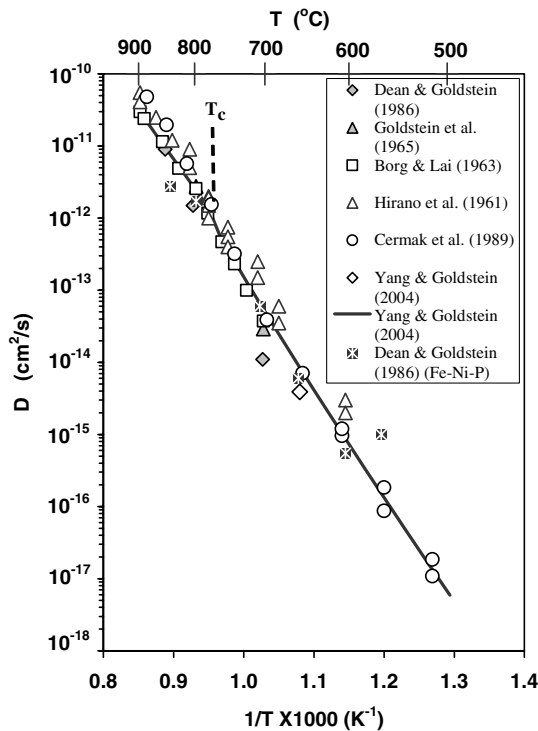
Fig. 6. Temperature dependence of the interdiffusion coefficients in bcc binary Fe–Ni and ternary Fe–Ni–P alloys. All the data are for the binary Fe–Ni system except data from Dean and Goldstein (1986). T_c is the Curie temperature.

Yang and Goldstein (2004) developed a new method, which utilizes the effect of magnetic ordering on physical, magnetic and mechanical properties of Fe–Ni alloys, to calculate interdiffusion coefficients in kamacite as a function of temperature. The Yang and Goldstein (2004) calculated results are consistent with the most recent experimental diffusion measurements (Cermak et al., 1989), and are used in the numerical model.

Taenite interdiffusion coefficients have been determined experimentally (Goldstein et al., 1965; Dean and Goldstein, 1986) for the binary Fe–Ni system. These coefficients were fit by Saikumar and Goldstein (1988) and by Hopfe and Goldstein (2001) in their computer simulation models for Ni contents <50 wt%. In the current study, we employ the fit developed by Yang and Goldstein (2004) for Ni contents up to 70 wt% in binary Fe–Ni.

Dean and Goldstein (1986) showed experimentally that P has a significant effect on the interdiffusion coefficients in kamacite and taenite. Saikumar and Goldstein (1988) used the data of Dean and Goldstein (1986) to express the interdiffusion coefficients as a function of the ratio of P in kamacite ($P_\alpha^{Fe-Ni-P}$) to the solubility limit of P in kamacite ($P_\alpha^{Sol.}$) and the ratio of P in taenite ($P_\gamma^{Fe-Ni-P}$) to the solubility limit of P in taenite ($P_\gamma^{Sol.}$). After replotting the interdiffusion coefficients in kamacite for binary Fe–Ni and for P bearing Fe–Ni (Fig. 6), we observed that the effect of P on the interdiffusion coefficient in kamacite was negligible. Accordingly, the interdiffusion coefficient equa-

tion for P bearing kamacite given by Saikumar and Goldstein (1988) is no longer valid and is replaced by

$$D_\alpha^{Fe-Ni-P} = D_\alpha^{Fe-Ni} \tag{3}$$

The interdiffusion coefficient equation in P bearing taenite, as developed by Saikumar and Goldstein (1988), was also re-evaluated. We found that the equation is valid and the equation will be employed in this study.

2.2.4. Numerical model

The numerical model simulates diffusion controlled kamacite growth in taenite for the Fe–Ni–P phase system. The cooling rate algorithm is based on the model developed by Hopfe and Goldstein (2001). The model uses the Murry and Landis (1959) variable grid spacing technique, the Crank and Nicolson (1947) approximation to describe the partial differential equation and the tridiagonal matrix algorithm (Von Rosenberg, 1969) to solve the appropriate difference equations. Plate morphology is assumed for the kamacite which nucleates and grows in one dimension consuming some of the matrix taenite. Ni is redistributed between kamacite and taenite and the growth process is controlled by the interdiffusion coefficients in kamacite and taenite and by the equilibrium Fe–Ni content as a function of temperature at the kamacite–taenite interface. A constant cooling rate is assumed for the temperature range in which the Widmanstatten pattern forms. The model includes the applicable mechanisms (II and V) for Widmanstatten pattern formation and the kamacite nucleation temperature (Section 2.2.1, Table 1) for each meteorite. The model also includes the equilibrium Fe–Ni and Fe–Ni (P sat.) phase diagrams (Section 2.2.2), and the binary and ternary diffusion coefficients (Section 2.2.3). Impingement is considered by varying the distance (L in the computer model) between adjacent kamacite plates. As L decreases, overlapping Ni gradients in the taenite between two kamacite plates are calculated. The central Ni content in taenite and the half-width of the taenite at a specific cooling rate are the output of the computer model used for calculating cooling rates by the Wood method (See Section 3). The model also yields Ni profiles in both the kamacite and taenite phases.

2.3. Compositional measurement

The meteorite samples were mounted in epoxy resin, ground with SiC papers of various grits (180, 240, 320, 400, and 600) and polished with diamond paste (6, 3, 1, and 0.25 μm). The samples were put in a glass container with ethyl alcohol or methanol and ultrasonically cleaned after each grinding or polishing step. The samples were carbon coated to ensure good electric conduction during analysis.

Quantitative WDS X-ray measurements were carried out using a Cameca SX-50 electron probe microanalyzer. An operating voltage of 15 kV and a beam current of 40 nA were

used. Two major elements (Fe and Ni) and two minor elements (Co and P) were measured. Pure Fe, Ni, Co, and $(Fe–Ni)_3P$ in the Grant meteorite were used as standards. Counting times for peak and background measurements were 30 s for Fe and Ni, 40 s for Co and 60 s for P.

We measured these four elements across taenite bands point by point along a line perpendicular to the kamacite–taenite interface in all the IIIAB samples. The distance from one measured point to the next was usually 1 μm except in wide taenite bands. For each meteorite, 8–25 taenite bands were measured. A typical M shape Ni profile was obtained across each taenite band. We measured the central taenite Ni content and the corresponding taenite half-width. Fig. 7a shows a back scatter electron image of a typ-ical taenite band. The analysis points across both the kamacite and taenite are observed. The Ni vs. distance profile measured from the microprobe trace, Fig. 7a, is shown in Fig. 7b. The taenite half-width is 40 μm. However, the actual taenite half-width, which is measured normal to the kamacite growth direction, is much smaller, 20 μm, after crystal orientation was considered. Methods to measure the actual half-width of the taenite band involve the determination of the kamacite/taenite band orientation with respect to the analyzed surface (Section 2.4).

2.4. Measurement of orientation between the sample surface and the kamacite–taenite interfaces of the Widmanstatten pattern

The two commonly observed orientation relations between the fcc-taenite and bcc-kamacite crystal structures in the characteristic Widmanstatten pattern are Nishiyama–Wasserman (N–W) and Kurdjumov–Sachs (K–S) (Nolze, 2004) in which a {111} fcc plane is parallel to a {110} bcc plane. When meteoritic samples are sectioned, polished, and etched to reveal the Widmanstatten pattern, the bcc kamacite bands on the sample surface are observed in four directions, sometimes three directions, and occasionally two directions. These directions represent the traces produced by {111} fcc planes of the high temperature taenite phase. If the adjacent traces of {111}γ planes on the sample surface form a rectangle or a square, the sample surface is parallel to one of the {100}γ planes and the angle between the sample surface and the {111}γ planes is 54.74°. If the adjacent traces of {111}γ planes on the sample surface form an equilateral triangle, the sample surface is parallel to one of the {111}γ planes and the angle between the sample surface and the other {111}γ planes is 70.53°.

In most cases, the sample is cut at an unknown orientation to the Widmanstatten pattern. Therefore, one must obtain the orientation of the kamacite–taenite interface to the sample surface. Three methods can be employed to obtain the orientation. The first two methods are light optical microscope techniques, one based on the operations of traces of {111}γ planes in two surfaces and the other one based on operations of traces of {111}γ planes in one surface. The third method is based on the measurement of poles of bcc planes using electron backscatter diffraction (EBSD). All three methods were used in this study and are described in the following subsections.

2.4.1. Crystal orientation determined by traces in two surfaces

This method requires two adjacent surfaces in order to determine the crystal orientation. One surface is called the primary surface (PS) on which the crystal orientations and chemical composition are measured. The other surface is called the auxiliary surface (AS). The two surfaces are ground, polished using standard metallographic
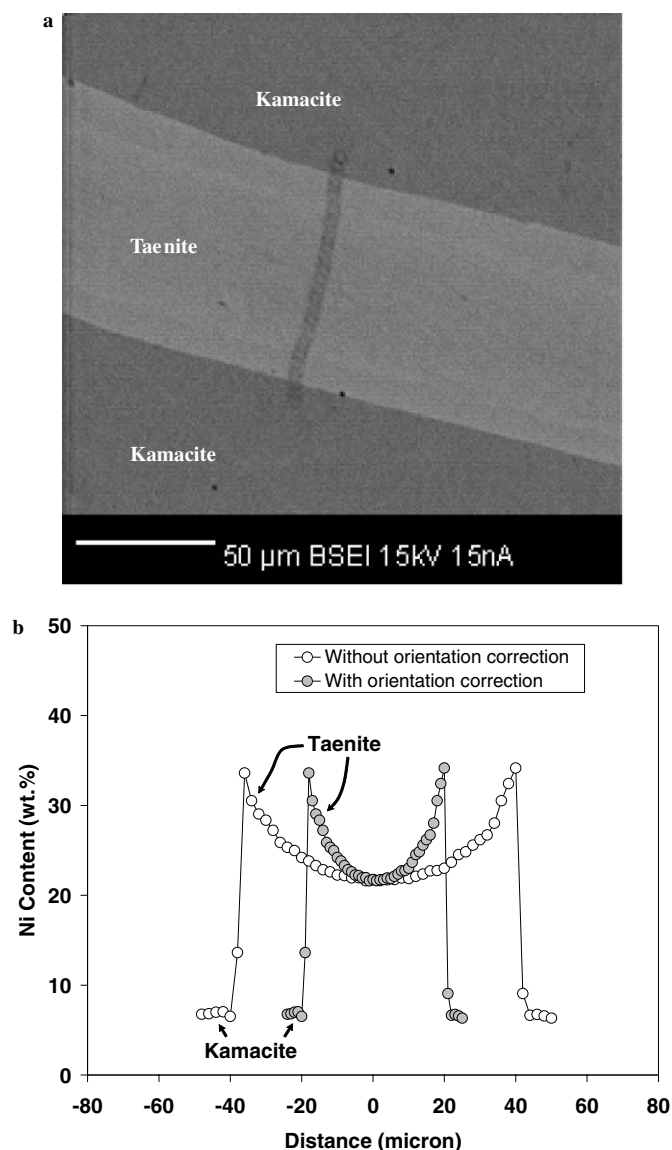

Fig. 7. (a) Back scatter electron image of a taenite band in the Bella Rock IIIAB iron showing the analysis line after electron probe microanalysis. (b) Ni vs. distance measurement along the analysis line across the taenite both before and after the correction for kamacite–taenite orientation.

techniques, and etched using 2% nital. The Widmanstatten structure on both the primary and the auxiliary surfaces are revealed and can be observed using optical microscopy. We measure two angles: the angles (β_1, β_2) between the edge, the connecting line between the primary and auxiliary surfaces, and the traces (representing the same $\{111\}\gamma$ planes on both primary and auxiliary surfaces), Fig. 8a and b. In addition, we measure the angle (α) between the primary and auxiliary surfaces, usually 90°. The measured angles are plotted on a stereographic net (Wulff net) and the poles of $\{111\}\gamma$ planes are determined using the method described by Barrett and Massalski (1966). An example is shown in Fig. 8d in which the poles of the $\{111\}\gamma$ planes of the IIIAB meteorite Bella Roca are plotted. In this figure, the great circle represents the primary surface and the center point of the great circle is the sample surface normal. This method works relatively well provided that the traces on both the primary and auxiliary surfaces can be clearly observed.
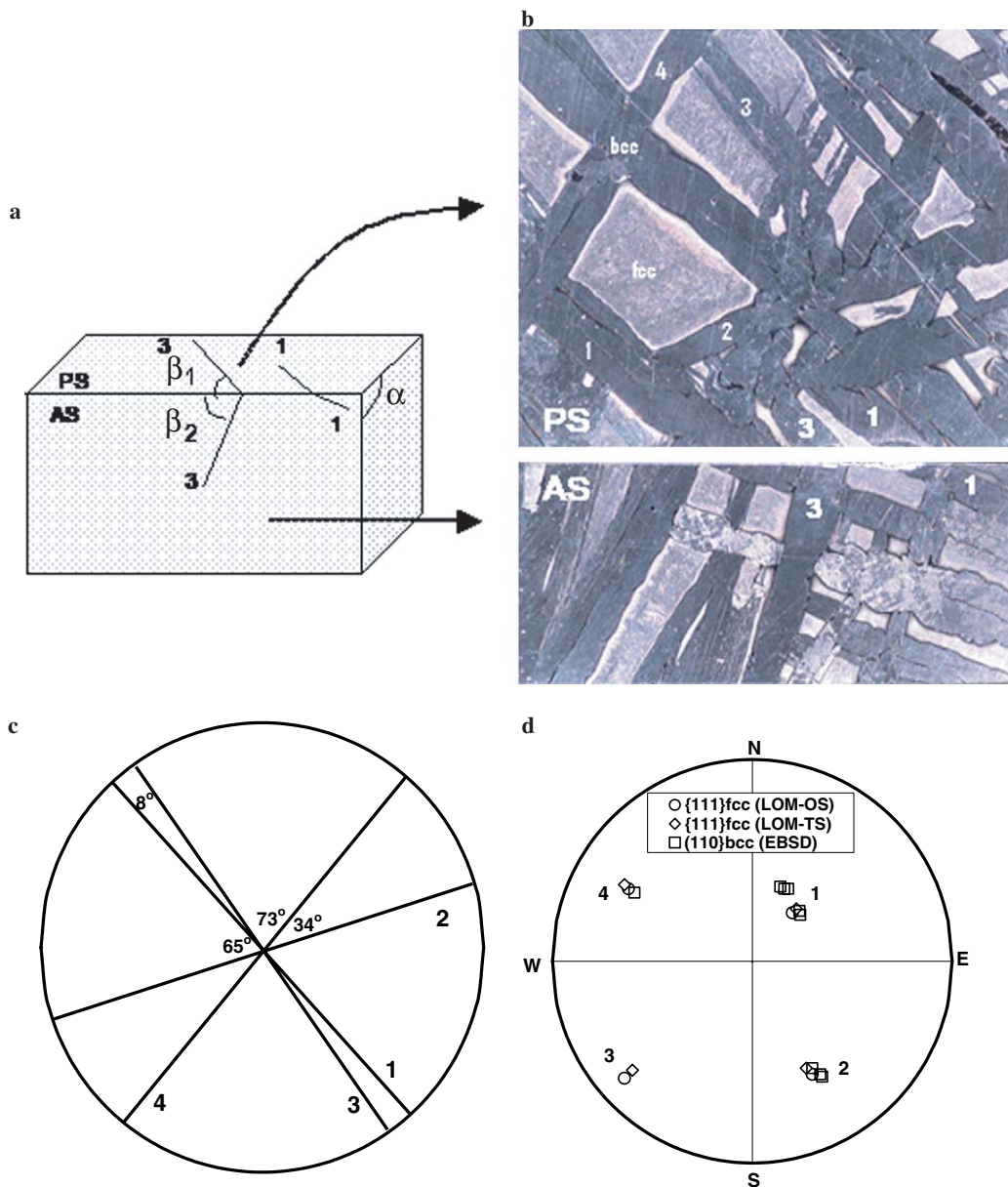

Fig. 8. Crystal orientation methods applied to the IIIAB iron Bella Roca. (a) Schematic of the sample showing both the primary surface (PS) and the auxiliary surface (AS). (b) Widmanstatten pattern observed by light optical microscopy on the primary surface and on the auxiliary surface. Widmanstatten plates of the same orientation are numbered on both surfaces. (c) Angles between traces 1, 2, 3, and 4 of the Widmanstatten pattern. (d) Pole figure (stereographic projection) with orientation measurements by the three methods, o represents poles of $\{111\}$fcc obtained by the one surface method, symbol ◇ represents poles of $\{111\}$fcc obtained by the two surface method, and symbol □ represents poles of $\{110\}$bcc obtained by the one surface method using EBSD. The numbers represent either the traces of either the $\{111\}$fcc planes or the $\{110\}$bcc planes.

2.4.2. Crystal orientation determined by traces in one surface

Traces revealed by optical microscopy on one surface can be used to determine the crystallographic orientation. This method uses the procedure given by Drazin and Otte (1964). In order to use this method, three or four traces must be observed on the primary surface using optical microscopy. The angles between traces are measured first. The two smallest pairs of adjacent (acute) angles between the three traces are used to determine the orientation by an analytical method or by referring to the Table given by Drazin and Otte (1964).

An example of the use of this method is shown in Fig. 8b for the IIIAB meteorite Bella Roca. Starting with the smallest angle and proceeding counterclockwise, the angle measured between the traces 1–3 is 8°, 1–2 is 65°, 2–4 is 34°, and 3–4 is 73° (Fig. 8c). If we choose 8° and 65° as a pair, the Table by Drazin and Otte (1964) gives two possible surface normals. However, only one surface normal leads to the measured trace angle of 73°. Based on the formula given by Drazin and Otte (1964), we can identify four specific {111} planes, (111), ($\bar{1}$11), (1$\bar{1}$1) and (11$\bar{1}$). The positions of the poles of four γ-fcc {111} planes are shown in Fig. 8d. The advantage of this method is that only one surface is needed. The disadvantage is that the method requires very accurate measurement of angles between the traces.

2.4.3. Crystal orientation determined by traces in one surface using EBSD

Electron backscatter diffraction can be used to determine the crystallographic orientation on one surface as described by Randle (2003) and Schwarts et al. (2000). The measurement includes several steps: sample preparation, SEM-EBSD set-up, data collection, data processing, and data representation. Fig. 8d shows a few {110}α poles of bcc-kamacite measured on the IIIAB meteorite Bella Roca by EBSD.

A comparison of the poles of {111}γ planes, obtained by the two surface method, the one surface method, as well as the poles of {110}α planes obtained by EBSD can be seen in Fig. 8d. The comparison shows that the three methods yield equivalent crystal orientations.

2.4.4. Application of crystal orientation to the measurement of taenite bandwidth

The orientations of the kamacite–taenite bands in the Widmanstatten pattern of the IIIAB iron meteorites were measured for all 14 meteorites (Table 1). The orientations are represented by pole figures similar to Fig. 8d for Bella Roca, which show four poles of the {111}γ plane. The angles between any pole of {111}fcc planes and the surface normal (center of great circle) are measured by rotating clockwise (or anticlockwise) the pole around the center of the great circle to the E–W axis (or N–S axis). The angle (θ) between the pole and the center of the great circle is obtained with the aid of a Wulff net. For example, the θ angles between the poles of {111}fcc planes 1, 2, 3, and 4 and the surface normal (the center of the great circle) in Fig. 8d are 30°, 55°, 79°, and 63°, respectively. After the θ angles are obtained, the actual half-width of the taenite bands (L_{act}) is calculated by multiplying the apparent half-width of the taenite band (L_{app}) measured on the sample surface by $\sin(\theta)$, i.e., $L_{act} = L_{app} (\sin(\theta))$. For the taenite band shown in Fig. 7, the θ angle is 30°. Using this θ value and the measured half-width of the taenite band of 40 μm we calculate an orientation corrected taenite half-width of 20 μm.

3. Results—cooling rates of IIIAB magmatic irons

The Wood method (Wood, 1964) was used to determine the cooling rate of each IIIAB meteorite. We plotted the measured taenite central Ni content vs. the orientation-corrected taenite half-width for all analyzed bands in each IIIAB meteorite (Fig. 9). The calculated cooling rate curves from the metallographic cooling rate model (Section 2.2) were also plotted for each of the 14 IIIAB irons (Fig. 9). The measured taenite central Ni content vs. taenite half-width (corrected) data for each meteorite should fall along a calculated iso-cooling rate curve and a unique cooling rate should be obtained for each IIIAB iron.

Using the measured data and the calculated cooling rate curves, 8–25 distinct cooling rates were measured for each meteorite. For example, we measured 18 taenite bands in the Casas Grandes meteorite (Fig. 9). Data from the 18 bands yield 18 specific cooling rates. The measured cooling rate range, which represents the lowest and the highest measured cooling rates, is 60–195 °C/My. The cooling rate variation, defined as the ratio of the highest to the lowest measured cooling rate, is 3.25. The cooling rate range and the cooling rate variation for the 14 IIIAB iron meteorites are listed in Table 3.

We also calculated the logarithmic average cooling rate and the logarithmic two standard deviation of the logarithmic average cooling rate for each meteorite studied. For example, the logarithmic average of the 18 measured cooling rates for Casas Grandes is 2.01 and the two standard deviation of the logarithmic average cooling rate is ±0.38. The logarithmic two standard deviation of ±0.38 represents the uncertainty of the measurement of the logarithmic average cooling rate. The logarithmic average cooling rate of 2.01 for Casas Grandes is equal to a cooling rate of 102 °C/My (Table 3). The logarithmic two standard deviation of ±0.38 is equivalent to a 2σ uncertainty factor of 2.4. The 2σ uncertainty range of the cooling rate for Casas Grandes can be calculated using the 2σ uncertainty factor of 2.4. The 2σ uncertainty range of the cooling rate for Casas Grandes falls between the average cooling rate of 102 °C/My divided by the 2σ uncertainty factor of 2.4 and the average cooling

rate of 102 °C/My multiplied by the 2σ uncertainty factor of 2.4 (42.5–245 °C/My). Using the same procedure employed for Casas Grandes, we have calculated the average cooling rate, the 2σ uncertainty factor and the 2σ uncertainty range of the measured cooling rates for the 14 IIIAB meteorites (Table 3).

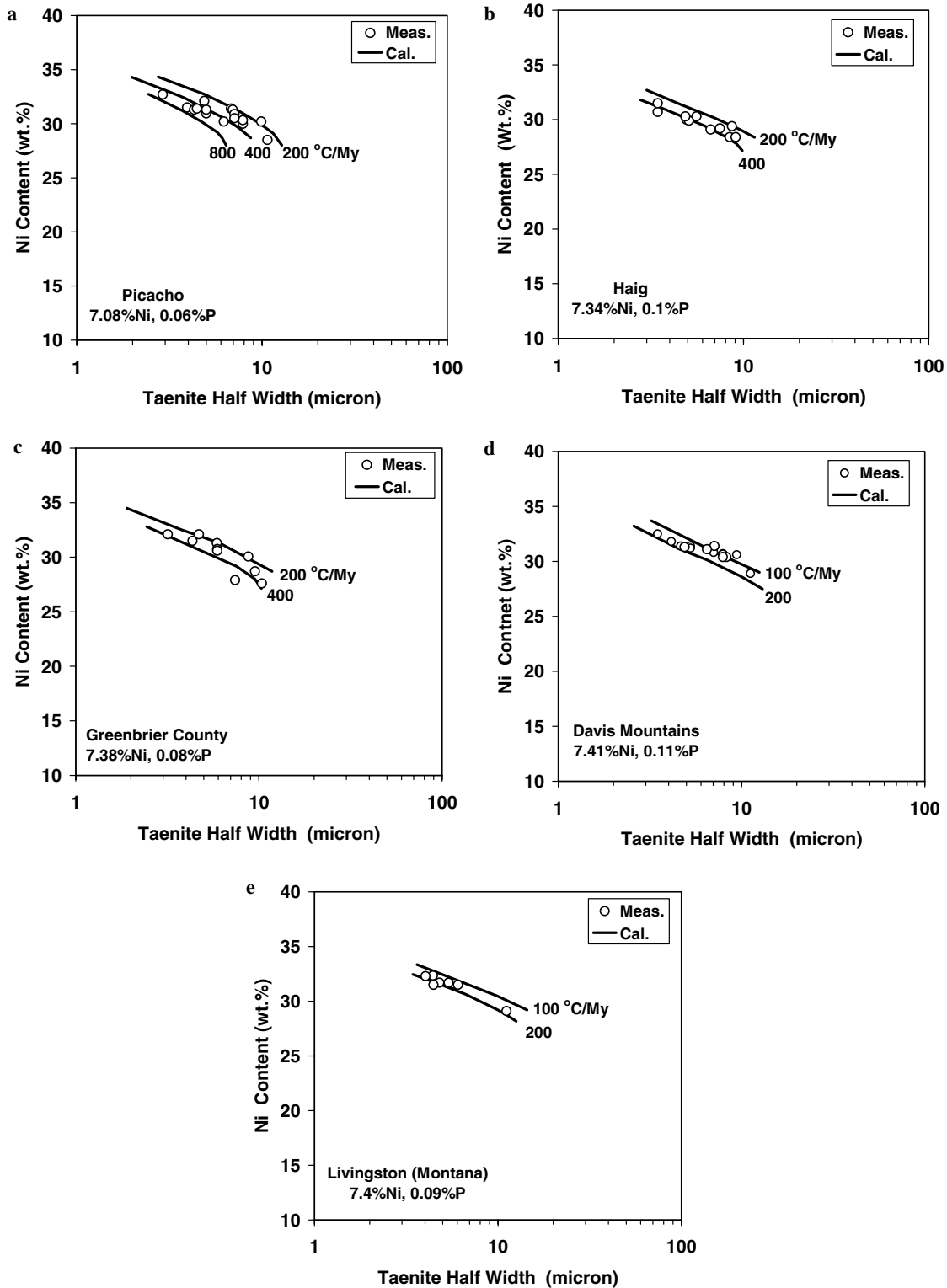Fig. 10 shows the measured metallographic cooling rate vs. the bulk Ni content of the 14 members of the IIIAB

Fig. 9. Central Ni content vs. taenite half-width, orientation corrected, data plotted for the 14 IIIAB irons. Calculated cooling rate curves are also plotted for each meteorite.
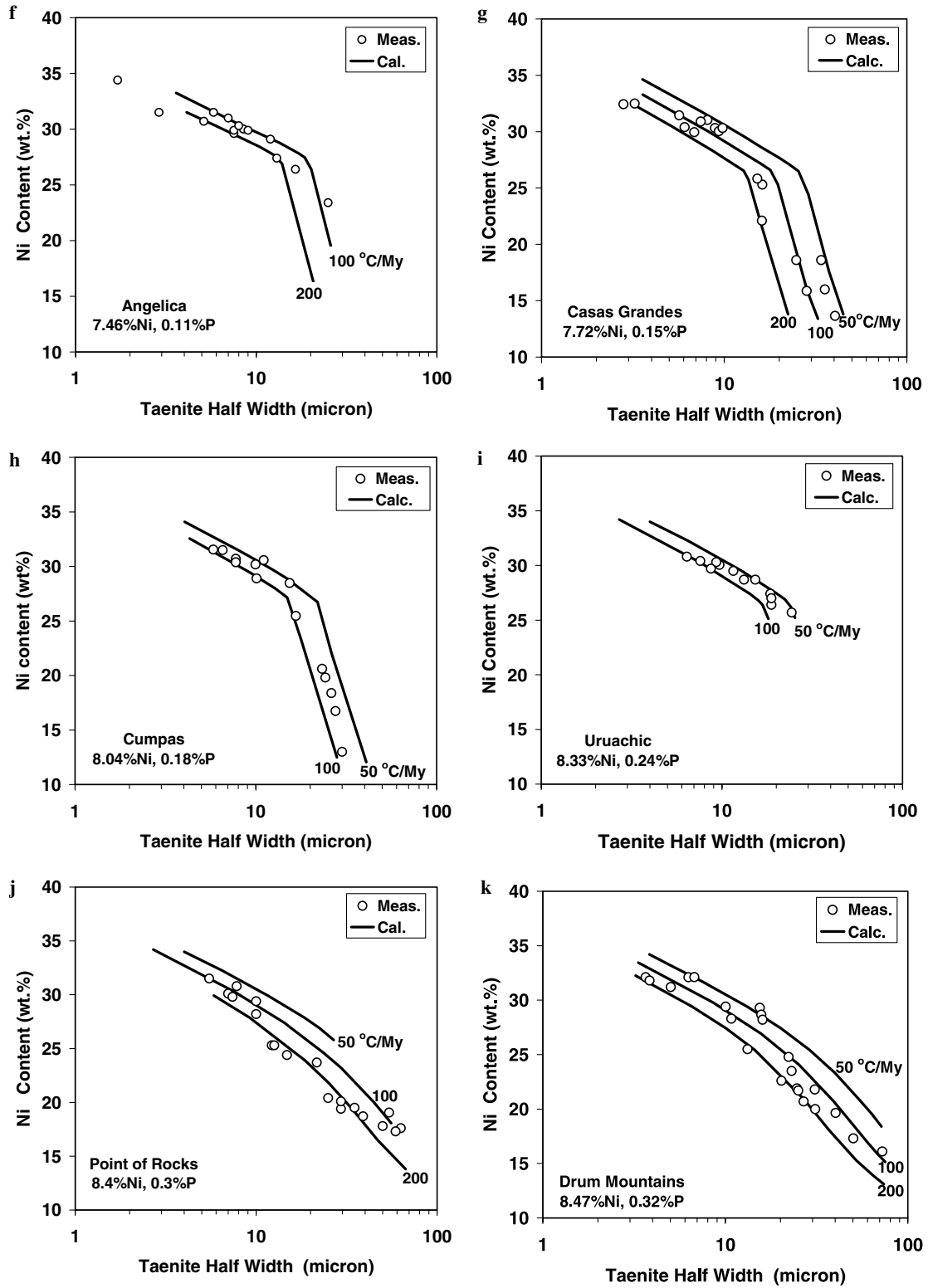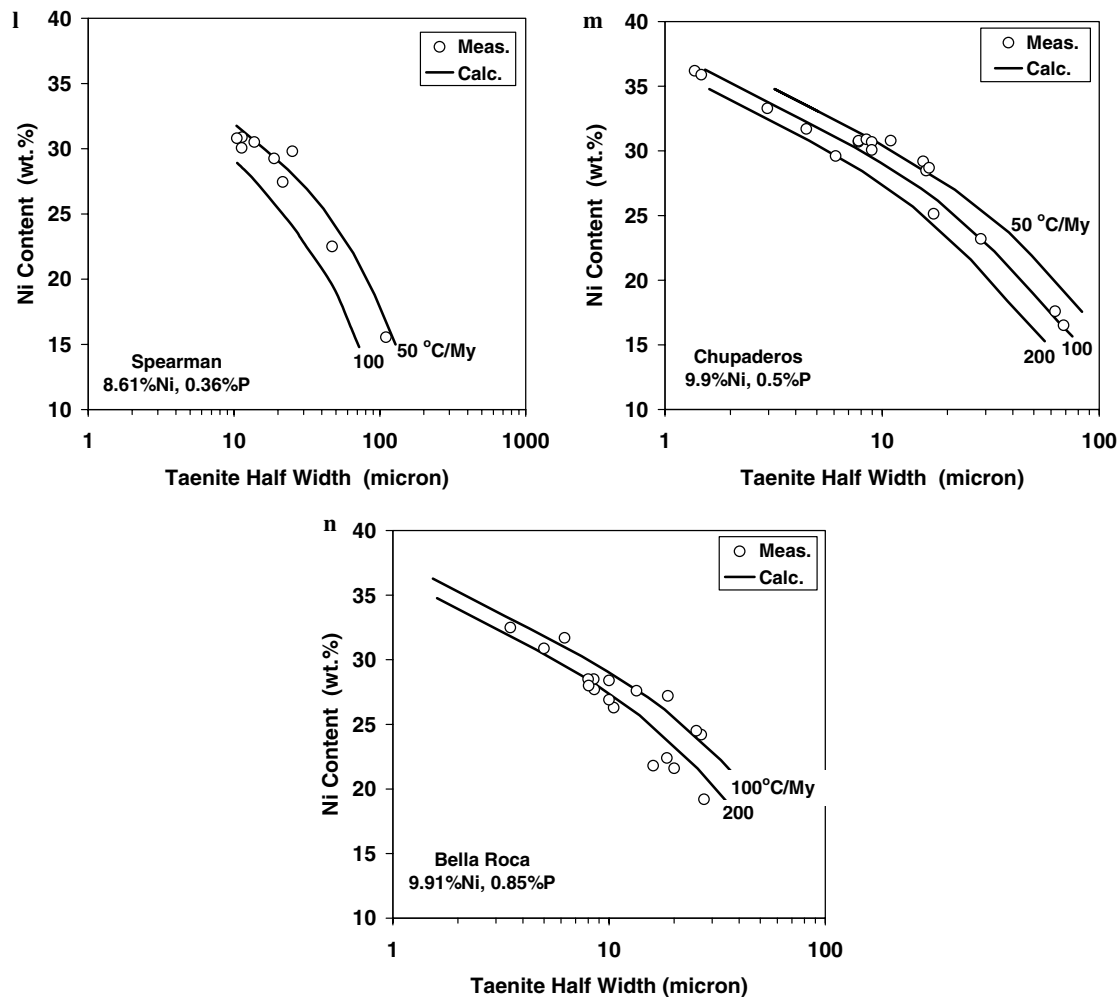
Fig 9. (*continued*)

Fig 9. (*continued*)

Table 3
Composition, measured cooling rate range, cooling rate variation, cooling rate, 2σ uncertainty factor and 2σ uncertainty range of 14 IIIAB meteorites

Meteorite name	Wt%Ni	Wt%P	CR range (°C/My)	CR variation	CR (°C/My)	2σ Uncertainty	2σ Uncertainty range (°C/My)
Picacho	7.08	0.06	190–600	3.1	338	2.14	158–723
Haig	7.34	0.1	200–500	2.5	331	1.62	204–536
Greenbrier County	7.38	0.08	200–600	3.0	291	1.99	146–579
Livingston (Montana)	7.4	0.09	70–175	2.5	113	1.88	60–212
Davis Mt.	7.41	0.11	135–210	1.5	160	1.38	115–220
Angelica	7.46	0.11	100–300	3.0	141	2.13	66–300
Casas Grandes	7.72	0.15	60–195	3.3	102	2.4	43–245
Cumpas	8.04	0.18	50–100	2.0	73	1.56	47–114
Uruachic	8.33	0.24	50–100	2.0	72	1.62	44–117
Point of Rocks	8.4	0.3	75–275	3.6	145	2.5	58–363
Drum Mt.	8.47	0.32	40–210	5.25	112	2.88	39–323
Spearman	8.61	0.36	35–70	2.0	56	1.51	37–85
Chupaderos	9.9	0.5	40–200	5.0	82	2.6	32–213
Bella Roca	9.91	0.85	75–400	5.3	162	2.82	57–457

chemical group. The cooling rates of the IIIAB irons vary from 338 to 56 °C/My and appear to vary inversely with Ni content from 7.1 to 8.6 wt%. The error bar for each meteorite in Fig. 10 represents the 2σ uncertainty range in the cooling rate (Table 3). Using the measured metallographic cooling rates for the 14 IIIAB irons, we calculate an average cooling rate of 132 °C/My with a large 2σ uncertainty range, from 42 to 409 °C/My (Fig. 10).
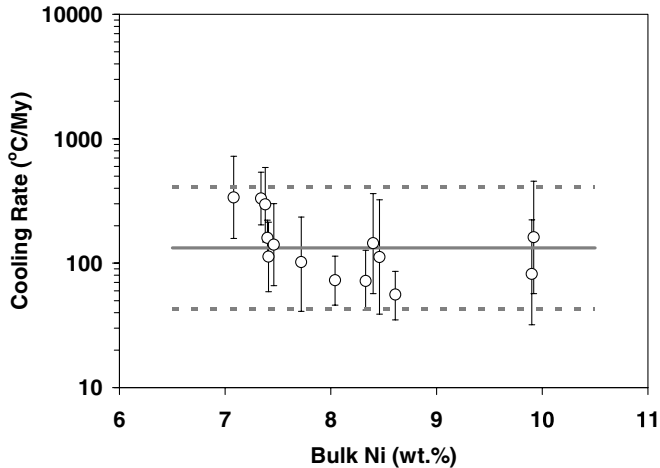
Fig. 10. Measured cooling rates vs. bulk Ni for 14 IIIAB irons. The error bar for each meteorite represents the cooling rate 2σ uncertainty. The solid line represents the average cooling rate and the two dashed lines represent the cooling rate 2σ uncertainty.

4. Discussion

4.1. Accuracy and uncertainty of the IIIAB metallographic cooling rates

4.1.1. Effect of kamacite phase boundary

Previous cooling rate studies have shown that cooling rate measurements are sensitive to the Ni content of the $\alpha/(\alpha + \gamma)$ phase boundary that is adopted for the cooling rate simulation (Willis and Wasson, 1978). In order to explore whether the cooling rates of the IIIAB irons are sensitive to the Ni content of the $\alpha/(\alpha + \gamma)$ phase boundary, the $\alpha/(\alpha + \gamma)$ phase boundaries (ALN, AUN) (Figs. 2 and 3a) used in this study were adjusted within the error limits of the experimentally determined Ni content of ALN and AUN as a function of temperature, Fig. 3a. A combination of the upper limit, maximum Ni content, of ALN (UALN) and AUN, and a combination of the UALN and the lower limit, minimum Ni content, of AUN (LAUN) were used to test the sensitivity of the cooling rate calculation to the Ni content of the $\alpha/(\alpha + \gamma)$ phase boundary. These two combinations for the Ni contents of the $\alpha/(\alpha + \gamma)$ boundary were substituted in the cooling rate model. The cooling rate calculations show that neither α phase boundary (UALN + AUN or UALN + LAUN) has an effect on the calculated cooling rate for high Ni members of the IIIAB irons. However, both the UALN + AUN and the UALN + LAUN combinations have a significant effect on the cooling rate calculation for low Ni members of the IIIAB irons. The changes in the $\alpha/(\alpha + \gamma)$ boundary, however, only allow the Widmanstatten pattern to grow to a very narrow thickness with a taenite half-width $\leqslant 6\ \mu m$ (Fig. 11). As shown in Fig. 11, only part of the calculated cooling rate curves using either the UALN + AUN or the UALN + LAUN combination matches the measured data. Therefore these two combinations of possible kamacite phase boundaries cannot be used to calculate
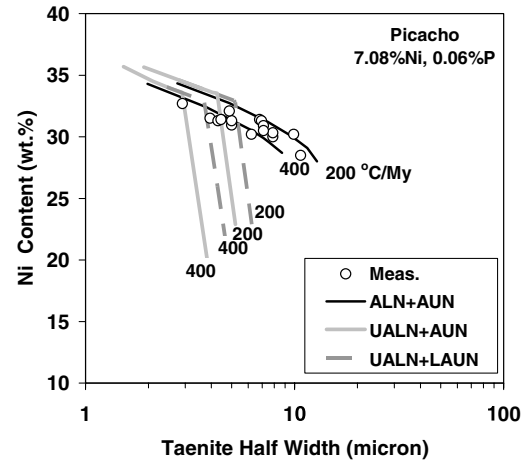

Fig. 11. Effect of varying $\alpha/(\alpha + \gamma)$ phase boundaries on the calculated cooling rates of the Picacho IIIAB iron.

appropriate cooling rate curves. The phase boundaries (ALN + AUN) used in this study (Section 2.2.2) result in very good matches between the calculated cooling rate curves and the measured data for the IIIAB meteorites (Fig. 9).

4.1.2. Effect of kamacite–taenite orientation

Goldstein and Short (1967) and Narayan and Goldstein (1985) did not take kamacite–taenite orientation effects into account in their IIIAB cooling rate measurements. Rasmussen (1989) used the two surface technique to determine the orientation of the Widmanstatten pattern. However, no detailed information was given about how the technique was applied or to what extent crystallographic orientation affected the cooling rate measurements.

The important role of kamacite–taenite orientation in the measurement of the cooling rate of meteoritic metal is illustrated by considering the data obtained for the Casas Grandes meteorite. Fig. 12a shows the measured central taenite Ni vs. taenite half-width data before kamacite–taenite crystal orientation is considered. Data from two sets of Widmanstatten bands, oriented 24° and 54° to the sample surface, are displayed. Cooling rates of 10–35 °C/My and of 40–200 °C/My are calculated for the two sets of kamacite–taenite bands oriented at 24° and 54°, respectively. As shown in Fig. 12a, it appears that each set of data has its own specific cooling rate and that the cooling rate variation is 20 when both sets of data are considered. After the effect of orientation is calculated, the two sets of data for Casas Grandes overlap and the cooling rates cluster much more tightly, between 60 and ~200 °C/My, a cooling rate variation of 3.3 (Fig. 12b).

Rasmussen (1989) also studied the Casas Grandes meteorite and determined that the cooling rate variation for this meteorite was 29.1 (Table 4). This cooling rate variation was even larger than the value of 20 obtained in this study before taking the effect of crystal orientation into account. It is possible that the large cooling rate variations measured
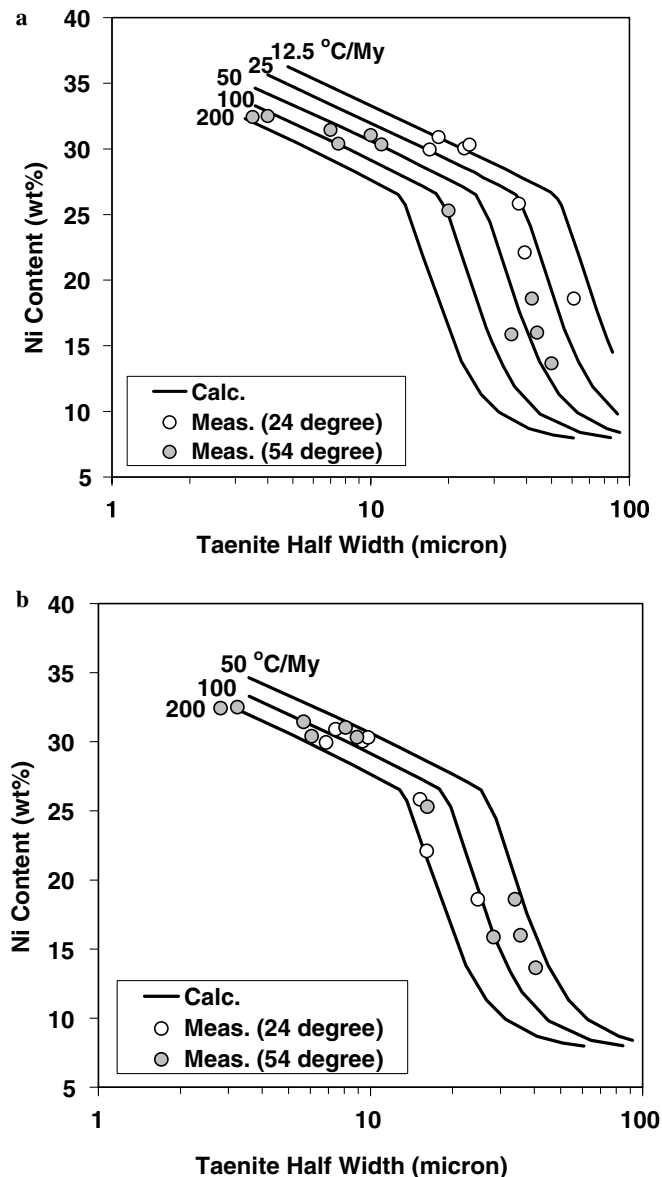
Fig. 12. Cooling rates of the IIIAB Casas Grandes meteorite (a) before and (b) after kamacite–taenite orientation effects are considered.

by Rasmussen (1989) for individual meteorites (Table 4) may be due to inaccuracies in orientation measurements.

Neglecting the crystal orientation in the cooling rate measurement not only leads to large cooling rate variations, but also leads to an inaccurate cooling rate value. The cooling rate for un-oriented kamacite–taenite interfaces will always be slower than the corrected value. Correcting for orientation effects will always reduce the measured taenite half-width and move the Ni data towards cooling rate curves with a higher cooling rate. For example the cooling rate determined from Fig. 12a for Casas Grandes from un-oriented kamacite–taenite interfaces is about 40 °C/My. After correction for orientation effects, the Ni data from the taenite bands oriented 24° to the surface move to smaller taenite half-widths and overlap the data from the taenite bands oriented 54° from the sample

surface (Fig. 12b). The Casas Grandes cooling rate determined from Fig. 12b, from orientation corrected taenite half-widths, is 102 °C/My (Table 2), an increase of 2.5 times the cooling rate obtained from un-oriented taenite bands.

4.1.3. Variability of cooling rate measurements

Table 4 lists the cooling rates, cooling rate ranges and cooling rate variations of the 14 IIIAB irons of this study and the 12 IIIAB irons of the Rasmussen (1989) study. Five meteorites from this study were also analyzed by Rasmussen (1989). In this study, the cooling rate variation for a given meteorite ranges from 1.5 to 5.3 with an average of 3.1. In the study by Rasmussen (1989), the cooling rate variation for a given meteorite ranges from 5 to 30 with an average of 14.4, almost 5 times larger than that in the current study (Table 4). Since the cooling rate variation for each meteorite is much smaller in this study, the uncertainty in the measured cooling rate for each meteorite is greatly reduced.

4.1.4. Accuracy of cooling rate measurements

The results of this study give an average cooling rate for a IIIAB core of 132 °C/My. Goldstein and Short (1967) obtained an average cooling rate of 5 °C/My and Rasmussen (1989) obtained an average cooling rate of 49 °C/My. The accuracy of the cooling rate measurements of Goldstein and Short (1967) and Narayan and Goldstein (1985) are in doubt. These authors used the kamacite bandwidth method to determine the cooling rate. Unlike the Wood (1964) method which include the impingement effect in the model (Sections 2.2.1 and 2.2.4), the kamacite bandwidth method neglects the effect of impingement which has occurred in all the IIIAB irons. Saikumar and Goldstein (1988) have shown that the metallographic cooling rate determined by the kamacite bandwidth method is inaccurate when compared to the use of the Wood method.

The average cooling rates of the IIIAB irons obtained in this study are >2.5 times higher than the cooling rates obtained by Rasmussen (1989). Both studies use the same basic approach to calculate the cooling rates and include the five major factors in the computer simulation (Section 2.2). Both computer simulations use the Wood method (Wood, 1964) and account for P effects in the Fe–Ni phase diagram and Fe–Ni diffusion coefficients. This study uses updated kamacite–taenite phase boundaries and diffusion coefficients. However, it is doubtful that the updated phase diagrams and diffusion coefficients are responsible for a major shift in the cooling rates using the Wood (1964) method. For example, the closure temperature below which the change of Ni content in the center of a taenite band is less than 0.25 wt% is about 400–450 °C. Most of the recent improvements in the phase diagrams are developed for temperatures at or below 450 °C.

It is not clear how the mechanism for Widmanstatten pattern formation and the kamacite nucleation temperature, used by Rasmussen (1989), differs from this study.

Table 4
Cooling rate comparison for IIIAB irons (this study, Rasmussen, 1989)

Meteorite name	Wt%Ni	Current study			Rasmussen (1989)		
		CR (°C/My)	CR range (°C/My)	CR variation	CR (°C/My)	CR range (°C/My)	CR variation
Picacho	7.08 (7.08)	338	190–600	3.1	185	90–600	6.6
Haig	7.34	331	200–500	2.5			
Greenbrier County	7.38	291	200–600	3.0			
Livingston (Montana)	7.4	113	70–175	2.5			
Davis Mt.	7.41	160	135–210	1.5			
Angelica	7.46	141	100–300	3.0			
Henbury	(7.47)				56	30–150	5.0
San Angelo	(7.52)				84	40–200	5.0
Casas Grandes	7.72(7.77)	102	60–195	3.25	53	12–350	29.1
Cumpas	8.04	73	50–100	2.0			
Uruachic	8.33	72	50–100	2.0			
Point of Rocks	8.4	145	75–275	3.6			
Drum Mt.	8.47(8.23)	112	40–210	5.25	21	5–110	22.0
Thule	(8.52)				22	5–110	22.0
El Capitan	(8.56)				52	12–150	12.5
Spearman	8.61	56	35–70	2.0			
Grant	(9.36)				57	19–120	6.3
Chupaderos	9.9(9.9)	82	40–200	5.0	49	16–250	15.6
Bella Roca	9.91(10.06)	162	75–400	5.3	44	22–110	5.0
Buenaventura	(9.95)				52	5–150	30.0
Tieraco Creek	(10.5)				24	5–60	12.0

Note: The Ni contents in the parentheses are from Rasmussen (1989).

Rasmussen (1989) used a combination of the pertinent phase diagram (Fe–Ni–P) and the local bulk Ni and P content to calculate these two factors. Neither study invokes the concept of undercooling. This study considers the two pertinent mechanisms for kamacite formation, (1) entering the $\alpha + \gamma + Ph$ three phase field during cooling or (2) martensite formation and subsequent decomposition into α-kamacite and γ-taenite. Unfortunately, the Rasmussen (1989) study does not list nucleation temperatures nor does it discuss the pertinent mechanisms for kamacite formation. Therefore, it is not possible to know in detail if the mechanism for Widmanstatten pattern formation and the kamacite nucleation temperature used by Rasmussen (1989) are substantially different and how they effect the cooling rate simulation. However, large variations in cooling rates were measured for each meteorite in the Rasmussen (1989) study. As discussed previously, it is possible that the large cooling rate variations measured by Rasmussen (1989) for individual meteorites (Table 4) may be due, in part, to inaccuracies in orientation measurements. As discussed in Section 4.1.2, neglecting the kamacite–taenite orientation in the cooling rate measurement not only leads to large cooling rate variations but to low values of the cooling rate. If orientation effects were not correctly handled, the Rasmussen (1989) IIIAB cooling rates will be too low.

4.2. IIIAB cooling rate variation

4.2.1. Relation to kamacite nucleation temperature

The cooling rate variation across the IIIAB chemical group is a factor of 6 in the current study, which is smaller than a factor of 10, Goldstein and Short (1967), 9, Narayan and Goldstein (1985), and 9, Rasmussen (1989). The results of this study give the smallest cooling rate variation measured across the IIIAB chemical group. However, a variation of 6 is still substantial given the much more limited variation in cooling rate measured for each meteorite. We assert that there is a real and measurable variation in the cooling rate across the IIIAB group.

The method for the determination of the nucleation temperature for the Widmanstatten pattern in the IIIAB irons was described in Section 2.2.1. The kamacite nucleation temperatures listed in Table 1 for the 14 IIIAB irons are plotted vs. bulk Ni in Fig. 13a. The kamacite nucleation temperature decreases about 45 °C as the Ni content increases from ~7 wt% to about 8.5 wt% and then abruptly increases about 100 °C at 8.5 wt% Ni. The kamacite nucleation temperature decreases about 50 °C as the Ni content increases from 8.5 wt% to about 10.0 wt%. The transition at 8.5 wt% Ni occurs as the kamacite nucleation mechanism changes from V ($\gamma \rightarrow \alpha_2 + \gamma \rightarrow \alpha + \gamma$) at low Ni contents to II ($\gamma \rightarrow \gamma + Ph \rightarrow \alpha + \gamma + Ph$) at high Ni. Since the majority of kamacite growth occurs in about the first 100 °C of cooling, one might expect that the measured cooling rates reflect the variation in nucleation temperature across the metal core of a parent body.

Fig. 13b shows the measured cooling rates of the IIIAB irons vs. Ni content. One can interpret these data as showing a decrease in cooling rates to about 8.5 wt% Ni, an increase to higher cooling rates at about 8.5 wt% Ni and an approximately constant cooling rate at higher Ni contents. A similar cooling rate trend can be observed in the IIIAB data of Rasmussen (1989) (see Fig. 13c and Table 4). The
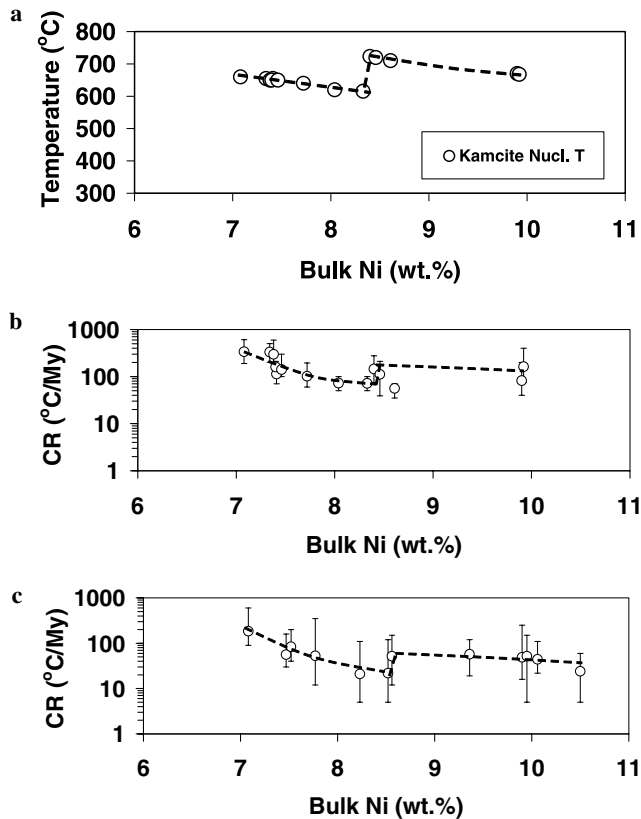
Fig. 13. (a) Variation of the kamacite nucleation temperature vs. Ni content for the 14 IIIAB irons. (b) Cooling rate variation vs. Ni content—current study. (c) Cooling rate variation vs. Ni content. Data from Rasmussen (1989). The error bar for each meteorite in (b and c) is the measured cooling rate range, Table 4.

cooling rate variation with Ni content across the IIIAB chemical group follows the kamacite nucleation temperature variation as described above (Fig. 13a).

If we assume the cooling rate vs. bulk Ni relationship follows the dashed line shown in Fig. 13b, we can use the residuals to compare this fit (Fig. 13b) with the fit assuming an average cooling rate (Fig. 10). We can also use the residuals to compare the fit of the Rasmussen cooling rate data (Fig. 13c) with the fit assuming an average cooling rate, (Fig. 4, Rasmussen, 1989). The residual for each meteorite is defined as the difference between the projected cooling rate obtained from the best fit dashed line and the measured cooling rate for each meteorite. The residual can be positive or negative depending on the relative position between the best fit dashed line and the measured cooling rate. We have measured the absolute value of each residual, added together the residuals for the 14 meteorites from the current study and calculated an average absolute residual. The average absolute residual is 34 °C/My based on the best fit line in Fig. 13b. The average absolute residual is 71 °C/My based on the assumption of a constant cooling rate line of 132 °C/My shown in Fig. 10. For the Rasmussen (1989) cooling rate data, the average absolute residual is 8 °C/My based on the best fit line for the 12 meteorites, Fig. 13c. The average absolute residual is 22 °C/My based

on the assumption of a constant cooling rate of 49 °C/My (Rasmussen, 1989). The best fit line of the varying cooling rates shown in Fig. 13b and c is significantly better than the assumption of an average cooling rate shown in Fig. 10 and in the Rasmussen (1989) study, Fig. 4.

Using thermal models of the asteroids, Haack et al. (1990) have shown that the cooling rate of the metal core at 700 °C is 1.3 times higher than the cooling rate at 500 °C. One might also expect a variation of this amount in the metallographic cooling rates of the IIIAB irons since the kamacite nucleation temperature varies by about 100 °C across the chemical group (Table 1). Clearly, the cooling rate variation predicted from the thermal model, ~1.3, is much less than the cooling rate variation of ~6 we have measured across the IIIAB chemical group (Table 1, Fig. 13). The concept of an average cooling rate for the IIIAB asteroidal core is not consistent with the measurements of this study. More sophisticated thermal models which include effects of shock impact, resulting, perhaps, in exposure of the metallic core to a complex cooling history, need to be developed.

4.2.2. Relation to cloudy zone formation

Yang et al. (1997b) developed an empirical cooling rate method to measure the cooling rate at temperatures below 400 °C. This method is based on the size of island phase formed in the cloudy zone region which borders the high Ni outer tetrataenite rim near the kamacite–taenite boundary. The formation of the cloudy zone is not related to the nucleation temperature of the Widmanstatten pattern and occurs at much lower temperatures. The size of island phase has been measured for four IIIAB irons, with Ni contents from 7.8 to 9.4 wt% (Yang et al., 1997b). The island phase sizes are similar, within ±10%, indicating a constant cooling rate through this part of the Ni range of the IIIAB irons. The metallographic cooling rates obtained in this study for meteorites with Ni contents from 7.8 to 9.4 wt% vary within a factor of 2.5 (Table 3 and Fig. 10). Given the uncertainty factor within two standard deviation (2σ) in the measurement of individual metallographic cooling rates of 1.5–2.6 (Table 3), we cannot say with any certainty that there is a variation in cooling rate in this Ni content range (7.8–9.4 wt% Ni). Unfortunately, there is no measurement of island phase sizes in the composition range, 7.1–7.8 wt% Ni, where there is a major change in the metallographic cooling rate (Table 3 and Fig. 10).

4.3. IIIAB parent body

4.3.1. Formation of IIIAB core

Iron meteorites are generally believed to experience several stages of development, condensation, oxidation and sulfurization, accretion, melting and segregation as well as solidification (Dodd, 1981). A parent body having experienced these stages would have a layered structure, in which dense metal iron phase would be located near the center and the light silicate phase would be located near the surface.

The separation of silicate and metal and the formation of the core are believed to occur rapidly very early after condensation. The short lived ^{182}Hf–^{182}W can serve to date the relative timing of silicate-metal separation or core formation (Horan et al., 1998), which is within 5 Ma for all magmatic iron groups. Therefore, the time for the formation of the IIIAB core is relatively short.

The solidification of isolated metal pools or a metal core would occur after separation from silicate. The long lived Re–Os system has been measured in several iron meteorites to determine the absolute age of crystallization (Horan et al., 1992, 1998; Smoliar et al., 1996). For IIIAB irons, an absolute crystallization age of 4558 Ma was obtained (Smoliar et al., 1996). The chemical element distribution patterns (Scott, 1972) and some isotope composition patterns such as Re–Os and Pt–Os (Cook et al., 2005) have been interpreted to be caused by the fractional crystallization process. However, recent Fe-isotope composition patterns in IIIAB irons (Mullane et al., 2005) are not systematic with respect to the fractional crystallization sequence and cannot be explained by assuming IIIAB irons are formed from a single crystallizing IIIAB magmatic core.

4.3.2. Possible IIIAB association with pallasites and other differentiated meteorites

Oxygen isotope data given by Clayton and Mayeda (1996) indicate that HED (howardites, eucrites, and diogenites) meteorites, mesosiderites, IIIAB irons, and main group pallasites (PMG) maybe derived from a single source. However, significant differences in cooling rates (Hutchison, 2004) suggest that either IIIAB irons, pallasites or mesosiderites were buried at far different depths within a single parent body or more probably they were formed in different parent bodies with very similar oxygen isotopes.

Minor and trace element distribution patterns in both IIIAB irons and PMG metal phase were interpreted as the result of fractional crystallization in the same parent body (Scott, 1977; Wasson and Choi, 2003). Moreover, PMG pallasites were assumed to be physically present between the metal core and mantle. There are still some problems, however, with the relationship between IIIAB irons and MPG pallasites. For example, if PMG pallasites are located between the metal core and mantle material, the metallographic cooling rates of the pallasites are expected to be very similar to those of the IIIAB metal core. Metallographic cooling rates (Buseck and Goldstein, 1968), though now outdated, showed that the cooling rates of the pallasites were slower than those of the IIIAB irons. Yang et al. (1997b) determined that the size of the island phase in the cloudy zone of the pallasites is around 3 times larger than that in IIIAB irons. This result implies that the cooling rate of the pallasites is significantly slower than that of the IIIAB irons. In addition, Re–Os data for IIIAB irons and for pallasites showed that the formation of pallasites appeared to be 60 My younger than for the IIIAB

irons (Chen et al., 2002). Given these data, it is very hard to reconcile the argument that pallasites are located at the boundary of the IIIAB irons.

4.3.3. Thermal history of the IIIAB parent body

Thermal models of differentiated asteroids, for example Haack et al. (1990), assume that the asteroid has a layered structure, which is regolith, crust, mantle and metallic core. In addition, these thermal models assume that the diameter of the parent body and structure of the parent body did not change during cooling from high temperature to low temperature. This assumption implies that no materials were lost or gained during cooling. Calculations using this type of thermal model (Haack et al., 1990) indicate that the cooling rate across the metallic core does not vary. Clearly, a cooling rate variation from 56 to 338 °C/My, as measured in this study, cannot be obtained in a differentiated asteroid containing a regolith, crust and core.

It is possible that asteroids experienced multiple impacts before break-up. The multiple impacts would result in either accumulation of new materials on the surface of asteroids or the loss of materials in the areas of regolith, crust and possibly mantle. Bottke et al. (2006) discuss the formation of iron meteorites and infer from the large number of iron meteorite parent bodies (~90; Keil, 2000), the lack of associated achondrites and differentiated asteroids, the lack of asteroid families derived from the break up of differentiated asteroids, and dynamic modeling that the silicate mantles were largely separated from the iron cores during transit from their formation location at 1–2 AU to the asteroid belt. Metal and silicate could have been separated by catastrophic impacts or tidal stripping during close approaches to embryos (Asphaug et al., 2006). If the IIIAB parent body had experienced multiple impacts above the Widmanstatten pattern formation temperature (~700 °C), it is possible that some materials would be lost from IIIAB parent body. The cooling rates obtained in the current study reflect the thermal history between 700 and 400 °C. As a result, the asteroid diameter at high temperatures could have been different from the diameter at low temperatures at which the metallographic cooling rate is measured. An exposed or partially exposed asteroidal core could have a cooling history where the cooling rate could vary by a factor of 6 as observed for the IIIAB irons of this study.

5. Conclusions

Metallographic cooling rates of 14 IIIAB irons have been measured and vary by a factor of 6 from 56 to 338 °C/My. The cooling rate variation for each meteorite is much smaller than in previous studies and the uncertainty in the measured cooling rate for each meteorite is greatly reduced.

Neglecting the orientation of the kamacite–taenite interface in the cooling rate measurement of a given meteorite not only leads to large cooling rate variations but to inac-

curate and correspondingly low cooling rates. The lack of orientation corrections may be responsible for the low cooling rate measurements in previous studies.

The cooling rates of the IIIAB irons follow the trend of the nucleation temperature of the Widmanstatten pattern with meteorite Ni content. The variation in the cooling rate across the IIIAB chemical group is attributable, in part, to the variation in nucleation temperature of the Widmanstatten pattern. However, the cause of most of the variation of a factor of 6 in cooling rate is hard to explain unless the IIIAB asteroidal core was exposed or partially exposed in the temperature range where the Widmanstatten pattern formed.

Large differences in the size of the island phase in the cloudy zone of the pallasites vs. IIIAB irons imply that the cooling rate of the pallasites and irons are significantly different. In addition, Re–Os data for IIIAB irons and for pallasites showed that the formation of pallasites appeared to be 60 My younger than for the IIIAB irons (Chen et al., 2002). Given these data, it is hard to reconcile the idea that pallasites are located at the boundary of the IIIAB irons.

Acknowledgments

Associate editor: Richard J. Walker

References

Asphaug, E., Agnor, C.B., Williams, Q., 2006. Hit-and-run planetary collisions. *Nature* **439**, 155–160.

Barrett, C.S., Massalski, T.B., 1966. *Structure of Metals: Crystallographic Methods, Principles, and Data Structure of Metals*. McGraw-Hill, New York.

Borg, R.J., Lai, D.Y.F., 1963. Diffusion of gold, nickel, and cobalt in alpha iron—a study of effect of ferromagnetism upon diffusion. *Acta Metall.* **11**, 861–866.

Bottke, W.F., Nesvorny, D., Grimm, R.E., Morbidelli, A., O'Brien, D.P., 2006. Iron meteorites as remnants of planetesimals formed in the terrestrial planet region. *Nature* **439**, 821–824.

Buchwald, V.F., 1975. *Handbook of Iron Meteorites. Their History, Distribution, Composition and Structure*. University of California Press, Berkeley and Los Angeles, CA.

Buseck, P.R., Goldstein, J.I., 1968. Pallasitic meteorites—implications regarding deep structure of asteroids. *Science* **159**, 300–302.

Cermak, J., Lubbehusen, M., Mehrer, H., 1989. The influence of the magnetic phase-transformation on the interdiffusion of Ni-63 in alpha-iron. *Z. Metallkd.* **80**, 213–219.

Chen, J.H., Papanastassiou, D.A., Wasserberg, G.J., 2002. Re–Os and Pd–Ag systematics in group IIIAB irons and in pallasites. *Geochim. Cosmochim. Acta* **66**, 3793–3810.

Clarke, R.S., Goldstein, J.I., 1978. Schreibersite growth and its influence on the metallography of coarse-structured iron meteorites. *Smithsonian Contrib. Earth Sci.*.

Clayton, R.N., Mayeda, T.K., 1996. Oxygen isotope studies of achondrites. *Geochim. Cosmochim. Acta* **60**, 1999–2017.

Cook, D.L., Walker, R.J., Horan, M.F., Wasson, J.T., Morgan, J.W., 2005. Pt–Re–Os systematics of group IIAB and IIIAB iron meteorites. *Geochim. Cosmochim. Acta* **68**, 1413–1431.

Crank, J., Nicolson, P.A., 1947. Practical method for numerical evaluation of solutions of partial differential equations of the heat-conduction type. *Proc. Camb. Philos. Soc.* **43**, 50–67.

Dean, D.C., Goldstein, J.I., 1986. Determination of the interdiffusion coefficients in the Fe–Ni and Fe–Ni–P systems below 900 °C. *Metall. Trans.* **17A**, 1131–1138.

Doan A.S., Goldstein J.I., 1969. The formation of phosphides in iron meteorites. In: Peter M. Millman (Ed.), *Meteorite Research. Proceedings of a Symposium on Meteorite Research*. Dordrecht, D. Reidel Publishing Company, pp. 763–779.

Doan, A.S., Goldstein, J.I., 1970. The ternary phase diagram, Fe–Ni–P. *Metall. Trans.* **1**, 1759–1767.

Dodd, R.T., 1981. *Meteorites, a Petrologic-Chemical Synthesis*. Cambridge University Press, New York.

Drazin, M.P., Otte, H.M., 1964. *Tables for Determining Cubic Crystal Orientations from Surface Traces of Octahedral Planes*. P.M. Harrod Co., Baltimore.

Goldstein, J.I., Ogilvie, R.E., 1965. A re-evaluation of the iron-rich portion of the Fe–Ni system. *Trans. Metall. Soc. AIME* **233**, 2083–2087.

Goldstein, J.I., Hunneman, R.E., Ogilvie, R.E., 1965. Diffusion in the Fe–Ni system at l atm and 40 kbar pressure. *Trans. TMS-AIME* **233**, 812–820.

Goldstein, J.I., Short, J.M., 1967. The iron meteorites, their thermal history and parent bodies. *Geochim. Cosmochim. Acta* **31**, 1733–1770.

Goldstein, J.I., 1969. The classification of iron meteorites. In: Peter M. Millman, (Ed.), *Meteorite Research. Proceedings of a Symposium on Meteorite Research*. Dordrecht, D. Reidel, pp. 721–737.

Haack, H., Rasmussen, K.L., Warren, P.H., 1990. Effects of regolith megaregolith insulation on the cooling histories of differentiated asteroids. *Geophys. Res.* **95B**, 5111–5124.

Hirano, K., Cohen, M., Averbach, B.L., 1961. Diffusion of nickel in iron. *Acta Metall.* **9**, 440–445.

Hopfe, W.D., Goldstein, J.I., 2001. The metallographic cooling rate method revised: application to iron meteorites and mesosiderites. *Meteorit. Planet. Sci.* **36**, 135–154.

Horan, M.F., Morgan, J.W., Walker, R.J., Grossman, J.N., 1992. Rhenium–osmium isotope constraints on the age of iron-meteorites. *Science* **255**, 1118–1121.

Horan, M.F., Smoliar, M.I., Walker, R.J., 1998. W-182 and Re-187–Os-187 systematics of iron meteorites: chronology for melting, differentiation, and crystallization in asteroids. *Geochim. Cosmochim. Acta* **62**, 545–554.

Hutchison, R., 2004. *Meteorites: a Petrologic, Chemical and Isotopic Synthesis*. Cambridge University Press, Cambridge.

Keil, K., 2000. Thermal alteration of asteroids: evidence from meteorites. *Planet. Space Sci.* **48**, 887–903.

Moren, A.E., Goldstein, J.I., 1979. Cooling rates of group IVA iron meteorites determined from a ternary Fe–Ni–P model. *Earth Planet. Sci. Lett.* **43**, 182–196.

Mullane, E., Russell, S.S., Gounelle, M., 2005. Fractionation of iron isotopes during magmatic processing on the IIIAB parent body. *Meteorit. Planet. Sci.* **40**, S108.

Murry, W.D., Landis, F., 1959. Numerical and machine solutions of transient heat-conduction problems involving melting or freezing. part I-method of analysis and sample solutions. *Trans. ASME J. Heat Transfer* **81**, 106–112.

Narayan, C., Goldstein, J.I., 1985. A major revision of iron meteorite cooling rates—an experimental-study of the growth of the Widmanstatten pattern. *Geochim.Cosmochim. Acta* **49**, 397–410.

Nolze, G., 2004. Characterization of the fcc/bcc orientation relationship by EBSD using pole figures and variants. *Z. Metallkd* **95**, 744–755.

Randle, V., 2003. *Microtexture Determination and its Applications*, second ed. Maney for the Institute of Materials, Minerals and Mining, London.

Rasmussen, K.L., 1989. Cooling rates of IIIAB iron meteorites. *Icarus* **80**, 315–325.

Romig, A.D., Goldstein, J.I., 1980. Determination of the Fe–Ni and Fe–Ni–P phase diagrams at low temperatures (700 to 300 °C). *Metall. Trans.* **11A**, 1151–1159.

Romig, A.D., Goldstein, J.I., 1981. Low temperature phase equilibrium in the Fe–Ni and Fe–Ni–P systems: application to the thermal history of metallic phases in meteorites. *Geochim. Cosmochim. Acta* **45**, 1187–1197.

Saikumar, V., Goldstein, J.I., 1988. An evaluation of the methods to determine the cooling rates of iron meteorites. *Geochim. Cosmochim. Acta* **52**, 715–726.

Schwarts, A.J., Kumar, M., Adams, B.L., 2000. *Electron Backscatter Diffraction in Materials Science*. Kluwer Academic, New York.

Scott, E.R.D., 1972. Chemical fraction in iron meteorites and its interpretation. *Geochim. Cosmochim. Acta* **36**, 1205–1236.

Scott, E.R.D., 1977. Geochemical relationships between some pallasites and iron-meteorites. *Mineral. Mag.* **41**, 265–272.

Smoliar, M.I., Walker, R.J., Morgan, J.W., 1996. Re–Os ages of group IIA, IIIA, IVA, and IVB iron meteorites. *Science* **271**, 1099–1102.

Von Rosenberg, D.U., 1969. *Methods for the Numerical Solution of Partial Differential Equations*. American Elsevier Publishing Company inc., New York.

Wasson, J.T., Choi, B.G., Jerde, E.A., Ulff-Moller, F., 1998. Chemical classification of iron meteorites: XII. New members of the magmatic groups. *Geochim. Cosmochim. Acta* **62**, 715–724.

Wasson, J.T., Choi, B.G., 2003. Main-group pallasites: chemical composition, relationship to IIIAB irons, and origin. *Geochim. Cosmochim. Acta* **67**, 3079–3096.

Willis, J., Wasson, J.T., 1978. Cooling rates of group IVA iron meteorites. *Earth Planet. Sci. Lett.* **40**, 141–150.

Wood, J.A., 1964. The cooling rates and parent bodies of several iron meteorites. *Icarus* **3**, 429–459.

Yang, C.-W., Williams, D.B., Goldstein, J.I., 1996. A revision of the Fe–Ni phase diagram at low temperature. *J. Phase Equilibria.* **17**, 522–531.

Yang, C.-W., Williams, D.B., Goldstein, J.I., 1997a. Low-temperature phase decomposition in metal from iron, stony-iron, and stony meteorites. *Geochim. Cosmochim. Acta* **61**, 2943–2956.

Yang, C.-W., Williams, D.B., Goldstein, J.I., 1997b. A new empirical cooling rate indicator for meteorites based on the size of the cloudy zone of the metallic phases. *Meteorit. Planet. Sci.* **32**, 423–429.

Yang, J., Goldstein, J.I., 2003. An Improved Model to Determine the Cooling Rates of Mesosiderites and Iron Meteorites (abstract #1156). *34th Lunar and Planetary Science Conference*. CD-ROM.

Yang, J., Goldstein, J.I., 2004. Magnetic contribution to interdiffusion coefficients in bcc (α) and fcc (γ) Fe–Ni alloys. *Metall. Mats. Trans.* **35A**, 1681–1690.

Yang, J., Goldstein, J.I., 2005. The formation mechanism of the Widmanstätten Structure in meteorites. *Meteorit. Planet. Sci.* **40**, 239–253.